

# 3-D Adaptive AUV Sampling for Classification of Water Masses

Yaolin Ge , Jo Eidsvik , and Tore Mo-Bjørkelund

**Abstract**—Autonomous underwater vehicles with onboard computing units foster innovative approaches for sampling oceanographic phenomena. Feedback of observations via the onboard model for planning algorithms enable adaptive sampling for such robotic units. In this work, we develop, implement, and test an adaptive sampling algorithm for efficient sampling of water masses in a 3-D frontal system. Focusing on a river plume, salinity variations are used to characterize the water masses. A threshold in salinity is assumed to distinguish the ocean and river waters, so that excursions below the threshold define river waters. The onboard model builds on a Gaussian random field representation of the salinity variations in (north, east, depth) coordinates. This model is initially trained from numerical ocean model data, and then updated with data gathered by the vehicle sensor. The Gaussian random field model further allows closed-form expressions of the expected spatially integrated Bernoulli variance of the salinity excursion set, which is used to reward sampling efforts. Combining these results with forward-looking planning algorithms, we suggest a workflow for 3-D adaptive sampling to map river plume systems. Simulation studies are used to compare the suggested approach with others. Results of field trials in the Nidelva river plume in Norway are presented and discussed.

**Index Terms**—Adaptive sampling, autonomous underwater vehicles (AUVs), excursion sets (ES), path planning, river plume.

## I. INTRODUCTION

A RIVER plume is formed when the fresh water flowing out of the river encounters the saline water in the ocean [1]. When these two different water masses meet, they form a varying spatio-temporal boundary [2]. There have been increasing efforts using numerical models and data to investigate such phenomena in the past decades [3], [4], [5], [6], [7], [8].

Autonomous underwater vehicles (AUVs) with onboard sensors and computing resources provide rich opportunities for oceanographic sampling as they can calibrate numerical ocean model outputs with in situ data, and fill in the sampling resolution gaps at locations with large uncertainty [9], [10], [11], [12]. For

frontal regions such as river plumes, AUV sampling is helpful for classifying the different water masses more accurately. Previous AUV sampling efforts focus mainly on preprogrammed designs [13] or use event-triggered adaptation of designs [14], [15]. Recent efforts have shown added value of having model-based adaptive sampling plans [16]. Adaptive sampling strategies here refer to AUV planning schemes that enable the AUV plan to be updated based on the posterior knowledge from in situ sampling and the probabilistic model description. Ideas from statistical sampling design are highly useful in this field, because they can help guide the AUV to informative locations [16], [17].

The main contribution of this work is a 3-D full-scale adaptive AUV sampling strategy. With the AUVs limiting computing resources, a Gaussian random field (GRF) model serves as a statistical proxy models for the spatial salinity field in the 3-D domain (north, east, depth). This 3-D GRF model running onboard the AUV is sequentially refined using in situ observations. This refined probabilistic model is further a basis for evaluating AUV sampling designs. Starting with prior knowledge from a numerical ocean model, we use an AUV to adaptively explore the 3-D boundary between the water masses in the river plume. We suggest algorithms to speed up design computations and to enable efficient robotic maneuverability [18]. We use a statistical design criterion based on the uncertainty of the excursion set (ES) of low salinity which distinguishes the river from the ocean water. This ES is defined by spatial locations having salinity level below a user-defined threshold. Building on recently developed closed form expressions [16] for the expected integrated Bernoulli variance (EIBV) associated with the ES, we compare the EIBV associated with each candidate design location, and select the design which has the minimum EIBV. The EIBV is a useful criterion for improved classification of the river plume as it is large when probabilities of excursions are far from 0 and 1. One should select sampling designs that on expectation pull probabilities toward the 0 and 1 end-points to reduce the uncertainty of the ES.

Via simulation studies and in situ measurements from the Nidelva river plume in Trondheim, Norway, we study the properties of the EIBV sampling plans in the 3-D domain. For the real-world experiments we used a light AUV (LAUV) [19] with an on-board NVIDIA Jetson TX2 computing unit.

The rest of this article is organized as follows. In Section II, we provide the background and motivation for our work on adaptive AUV sampling to river plume water masses characterization. In Section III, we introduce the models and methods used in this article. In Section IV, we present our implementation used for

Manuscript received 10 February 2022; revised 2 November 2022; accepted 18 February 2023. Date of publication 26 April 2023; date of current version 14 July 2023. This work was supported by Norwegian Research Council (RCN) through the MASCOT project under Grant 305445. (Corresponding author: Yaolin Ge.)

**Associate Editor:** N. Cruz.

Yaolin Ge and Jo Eidsvik are with the Department of Mathematical Sciences, Norwegian University of Science and Technology, 7034 Trondheim, Norway (e-mail: yaolin.ge@ntnu.no; jo.eidsvik@ntnu.no).

Tore Mo-Bjørkelund is with the Department of Marine Technology, Norwegian University of Science and Technology, 7034 Trondheim, Norway (e-mail: tore.mo-bjorkelund@ntnu.no).

Digital Object Identifier 10.1109/JOE.2023.3252641

path planning. In Section V, we show a simulation study illustrating the properties of our 3-D adaptive sampling approaches. In Section VI, we show results from the Nidelva river plume experiments. Finally, Section VII concludes this article.

## II. OCEAN SAMPLING

### A. Data Sources

Numerical solutions of the complex differential equations governing spatio-temporal oceanographic variation with boundary conditions and forcing are essential in understanding the ocean variability. In our application we rely on a fjord-scale implementation of the SINMOD software [20]. Such ocean model data provide physical interpretability of the ocean variability, but they often need calibration or bias adjustments, and there have been growing interests in uncertainty quantification and data assimilation methods for various scales of this challenge, see, e.g., [21].

Traditional in situ measurements generating input or calibration data to numerical ocean models include stationary or floating buoys, gliders, moorings, and ships [22]. With the advent of smaller inexpensive sensor systems, one has capabilities of handling a variety of measurements for biological, chemical, and oceanographic purposes [22]. Ships data can be expensive, and buoys and gliders have limited flexibility in maneuverability given coverage constraints [23].

Satellite imagery has been a powerful and useful tool for analyzing ocean variables. Data from satellites can provide a large-scale coverage of the entire field of interest, and even output portraits of river plumes [6]. However, due to large latency and uncertainty (cloud coverage issues) of obtaining such images, the usage of satellite imagery is limited. Satellite data unfavorably cover only the surface of the ocean [24].

The development of underwater robotics have led to a large number of robot-assisted applications in oceanography. Thanks to the flexibility of the robots, there are growing numbers of autonomous sampling missions which are conducted by robots [9]. Benefits further include real-time sensing and high-resolution data gathering, with large opportunities to move in flexible paths in the ocean environment. In our case, an AUV is used as the target platform which is able to support 3-D adaptive sampling at high resolution.

### B. Sequential AUV Sampling

We denote the salinity field by  $\{\xi_{\mathbf{u}}; \mathbf{u} \in \mathcal{M} \subset \mathcal{R}^3\}$ , where the location  $\mathbf{u}$  is (longitude, latitude, depth) and  $\mathcal{M}$  is the spatial domain of interest. Initially, we specify a probabilistic model for the salinity based on numerical ocean model data. This provides a realistic initial model for the 3-D salinity characteristics, one that it is much more physically inspired than a simple linear regression from available in situ AUV data [16]. We still use regression analysis to calibrate the 3-D ocean model data to the real-world ocean experiment by using a short preliminary AUV survey [25]. The objective of the survey is not to reveal the entire field, but rather provide some in situ measurements to adjust

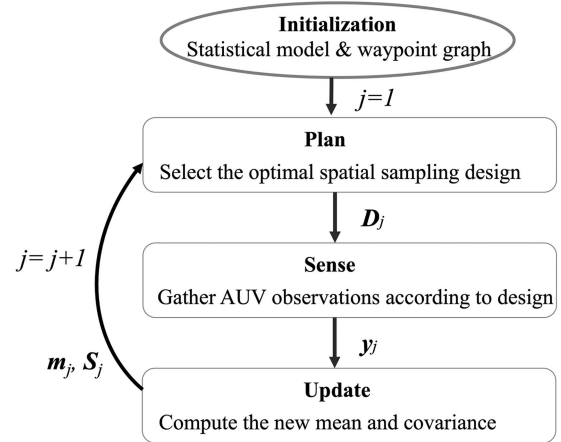


Fig. 1. Sequential loop where design  $D_j$  is chosen based on the updated model,  $y_j$  is the data collected in this design, and this is used to update the model  $(m_j, S_j)$ . This continues over stages  $j = 1, 2, \dots, J$ .

the ocean-model data and to form a reasonable prior model for the day of deployment. Therefore, the path for the preliminary survey can be as simple as a transect line with yo-yo movements in the vertical direction. As mentioned in the previous section, one can also use satellite data or even drone images in this initial model specification, if such data are available [26].

In situ salinity observations for the main part of the deployment are denoted by  $\{y_j; j = 1, \dots, J\}$ , for stages  $j$  of AUV measurements gathered over time. The vector  $y_j$  of measurements at stage  $j$ , holds  $N_j$  measurements made according to spatial sampling design  $D_j$ . The initial deployment location will then define  $D_1$ . We denote by  $\mathcal{Y}_j = \{(y_1, D_1), \dots, (y_j, D_j)\}$  the collection of data gathered with the selected designs up to stage  $j$ . Initially, this is an empty set;  $\mathcal{Y}_0 = \emptyset$ .

The sequential designs are selected adaptively based on what is evaluated to be the most informative AUV sampling locations. In this evaluation, the on-board model is conditional to all the data gathered until the current time. With new observations available, data assimilation methods are used to update the probabilistic representation for the salinity variables. This means that the model is “alive,” and changing at every stage, depending on the data. Adaptive sampling fits into the diagram loop in Fig. 1. In our setting the spatial design plan is optimized based on the current spatial statistical model. Then the AUV gathers new observations according to the chosen design, and the GRF model is updated. This continues over stages  $j = 1, \dots, J$ .

For prioritizing sampling efforts, one must impose an expected reward or value function associated with the different available sampling designs. At each stage, the expected rewards of all possible designs are evaluated. In our setting with river plumes, it makes sense to reward sampling locations that are expected to give data that improve the spatial characterization of the water masses [15], [16]. The setting is illustrated in Fig. 2, where we indicate the current location of the AUV, its path, and the sampling design opportunities at this stage. The information criterion (EIBV) is calculated for all feasible designs, shown as circular dots. Here, smaller dots with lighter colors are indicative

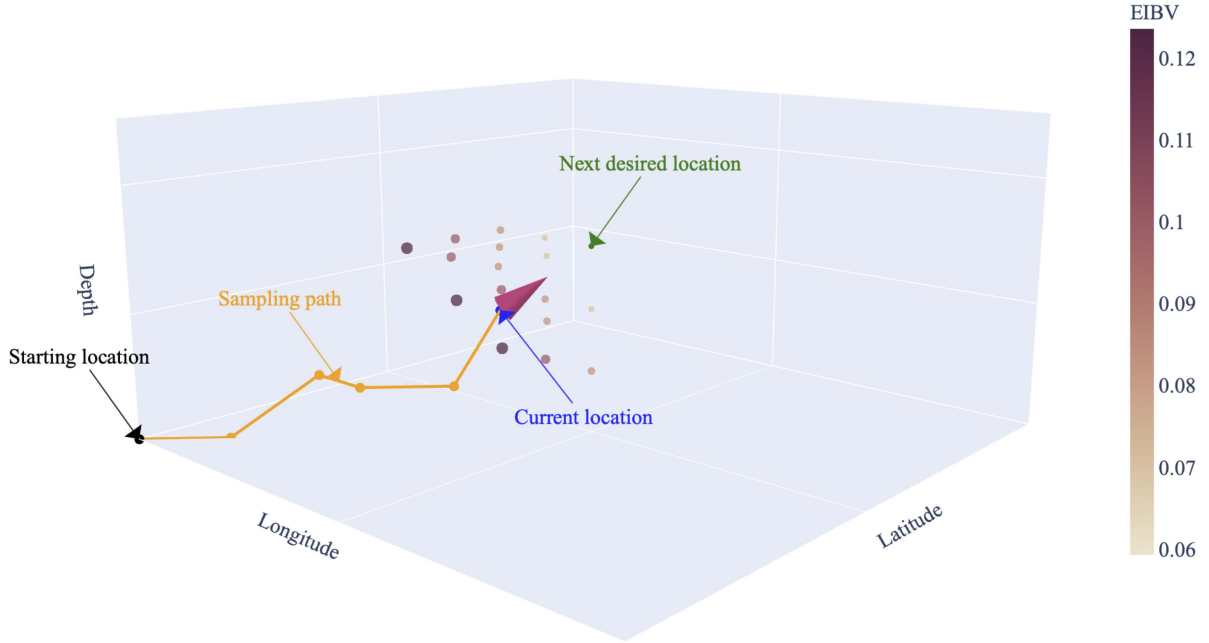


Fig. 2. Adaptive path example on a 3-D waypoint graph. There are 17 candidate locations in different layers, the blue dot shows the current AUV location whereas the green dot indicates the desired next waypoint selected based on the minimum EIBV criterion.

of larger expected uncertainty reduction. The adaptive sampling approach would act by moving to the location with lowest EIBV.

### III. STATISTICAL MODELS AND METHODS FOR AUV SAMPLING

We next discuss our probabilistic modeling choices for the salinity field, and show how this enables efficient data assimilation as well as onboard design criteria. We then define ES and the EIBV as a design criterion, and finally present an adaptive sampling design algorithm for efficient 3-D characterization of the river plume.

#### A. On-Board Computing With GRFs

The prior model for river plume salinity  $\{\xi_{\mathbf{u}}, \mathbf{u} \in \mathcal{M} \subset \mathcal{R}^3\}$ , is defined via a GRF. A working assumption in our work is hence that the GRF provides a reasonable proxy model for the spatial salinity field in (latitude, longitude, depth). The initial model specification includes estimating the expected value of the field, its variability and spatial dependence. Note that the duration of the experiment will be short and the temporal variation in the river plume is ignored here. To check the Gaussian assumption, we made a quantile-quantile (QQ) plot from the SINMOD salinity data (see Fig. 3). Here, we have computed the mean and variance at each location in a gridded domain over replicates of time steps. The standardized residuals are used in the QQ plot. The QQ plot in Fig. 3 shows a crossplot of the theoretical Gaussian quantile of the residuals against the empirical quantile of residuals in the data set. The blue line that we achieve is quite close to the straight line (red). Of course, the physical model does not give a Gaussian model, and we notice a sharper distribution near 0, but nevertheless the discrepancy is rather small.

Critically, the GRF model enables onboard data assimilation and adaptive AUV sampling efforts, as we will describe next.

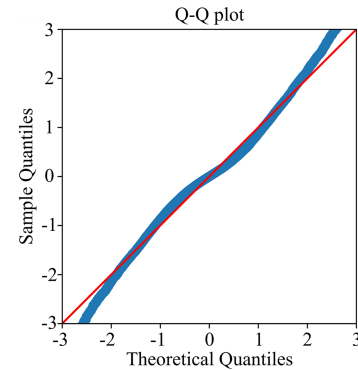


Fig. 3. Quantile-quantile plot of the residual based on SINMOD estimation. The residual is computed by subtracting the mean of the field and dividing the standard deviation.

For onboard implementation and computing, the spatial domain is discretized to a set of  $n$  grid locations;  $\{\mathbf{u}_1, \dots, \mathbf{u}_n\}$ . This grid is also used for the waypoint graph setting for the AUV sampling design. The prior or initial GRF model at these grid locations is denoted by

$$\boldsymbol{\xi} = (\xi_{\mathbf{u}_1}, \dots, \xi_{\mathbf{u}_n})^T, \quad \boldsymbol{\xi} \sim N(\boldsymbol{\mu}, \boldsymbol{\Sigma}) \quad (1)$$

with associated probability density function (PDF)  $p(\boldsymbol{\xi})$ . Here, length- $n$  vector  $\boldsymbol{\mu}$  represents the prior mean of the 3-D salinity variations, as will later be specified from ocean model data and a preliminary AUV transect run. The  $n \times n$  covariance matrix  $\boldsymbol{\Sigma}$  is defined via a Matérn covariance function with elements  $\Sigma(i, i') = \sigma^2(1 + \phi_1 h(i, i')) \exp(-\phi_1 h(i, i'))$ , where  $\sigma^2$  is the variance and  $\phi_1$  a correlation decay parameter [27]. The distance between grid nodes  $\mathbf{u}_i$  and  $\mathbf{u}_{i'}$  is defined for east, north, and depth Euclidean distances via

$$h^2(i, i') = h_E^2(i, i') + h_N^2(i, i') + (\phi_1^2/\phi_2^2)h_D^2(i, i')$$

with  $h$  being distance, and subscripts E, N, D indicating each of the three directions in vector  $\mathbf{u}_i - \mathbf{u}_i$ . Studies have shown that the lateral stretch of the river plume tends to be many magnitudes above the vertical stretch [1]. To model the correlation in different dimensions properly, we employ anisotropy between the lateral domain and the vertical domain. This means that the depth dimension is scaled differently ( $\phi_2$ ) using another correlation decay parameter than the one used in the lateral field ( $\phi_1$ ).

The measurements at each stage  $j = 1, \dots, J$  are modeled by a Gaussian likelihood model

$$\mathbf{y}_j | \boldsymbol{\xi} \sim N(\mathbf{F}_j \boldsymbol{\xi}, \mathbf{R}_j) \quad (2)$$

where  $\mathbf{F}_j$  is an  $N_j \times n$  selection matrix containing an entry of 1 in each row and 0 otherwise. The 1 entry refers to the sampling indices. With the covariance matrix  $\mathbf{R}_j = r^2 \mathbf{I}_{N_j}$ , we assume that the data are conditionally independent, given the underlying salinity. Here,  $r$  indicates the measurement standard deviation of the AUV salinity observations. We denote the associated PDF by  $p(\mathbf{y}_j | \boldsymbol{\xi})$ .

Via Bayes' rule, data assimilation at stages  $j = 1, \dots, J$ , gives the sequential conditional PDF  $p(\boldsymbol{\xi} | \mathcal{Y}_j) \propto p(\mathbf{y}_j | \boldsymbol{\xi}) p(\boldsymbol{\xi} | \mathcal{Y}_{j-1})$ . Under the assumptions about a GRF prior model and a Gaussian measurement error model, this conditional PDF is also Gaussian with mean  $\mathbf{m}_j$  and covariance matrix  $\mathbf{S}_j$  given by

$$\begin{aligned} \mathbf{G}_j &= \mathbf{S}_{j-1} \mathbf{F}_j^T (\mathbf{F}_j \mathbf{S}_{j-1} \mathbf{F}_j^T + \mathbf{R}_j)^{-1} \\ \mathbf{m}_j &= \mathbf{m}_{j-1} + \mathbf{G}_j (\mathbf{y}_j - \mathbf{F}_j \mathbf{m}_{j-1}) \\ \mathbf{S}_j &= \mathbf{S}_{j-1} - \mathbf{G}_j \mathbf{F}_j \mathbf{S}_{j-1} \end{aligned} \quad (3)$$

where  $\mathbf{m}_0 = \boldsymbol{\mu}$  and  $\mathbf{S}_0 = \boldsymbol{\Sigma}$ . The sequential updating resembles that of a spatio-temporal Kalman filter [27]. In our case, we study the benefits of using a 3-D spatial model in the AUV sampling. Having a relatively short-term deployment, no explicit temporal dynamics are modeled.

### B. Excursion Set and Expected Integrated Bernoulli Variance

We use the notion of an ES to characterize the river and ocean water masses [16]. The ES for salinity threshold  $t$  is defined by

$$\text{ES} = \{\mathbf{u} \in \mathcal{M} : \xi_{\mathbf{u}} \leq t\}. \quad (4)$$

Hence, salinity lower than this threshold will indicate river water. The associated excursion probability (EP) is

$$p_{\mathbf{u}} = P(\xi_{\mathbf{u}} \leq t), \quad \mathbf{u} \in \mathcal{M}. \quad (5)$$

When it is close to 1 or 0 at a given location, it is easy to classify the water mass to be river or ocean respectively. EP close to 0.5 reflects ambiguity in the characterization of water masses. The prior Bernoulli variance (BV) at location  $\mathbf{u}$  is  $p_{\mathbf{u}}(1 - p_{\mathbf{u}})$  and the spatially integrated BV (IBV) is

$$\text{IBV} = \int p_{\mathbf{u}}(1 - p_{\mathbf{u}}) d\mathbf{u} \quad (6)$$

which is dominated by locations with probabilities near 0.5 and BV close 0.25. In practice, the integral will be approximated by a sum over the  $n$  grid nodes.

The goal is to construct AUV sampling strategies that prioritize locations that are ambiguous, thus, making the exploration more effective. At each stage, we define the EIBV by

$$\begin{aligned} \text{EIBV}(\mathbf{D}_j) &= \int E_{\mathbf{y}_j | \mathcal{Y}_{j-1}; \mathbf{D}_j} [B_{\mathbf{u}}(\mathbf{y}_j)] d\mathbf{u} \\ B_{\mathbf{u}}(\mathbf{y}_j) &= p_{\mathbf{u}}(\mathbf{y}_j, \mathbf{D}_j, \mathcal{Y}_{j-1}) (1 - p_{\mathbf{u}}(\mathbf{y}_j, \mathbf{D}_j, \mathcal{Y}_{j-1})) \end{aligned} \quad (7)$$

where  $B_{\mathbf{u}}(\mathbf{y}_j)$  is the conditional Bernoulli variance for outcome  $\mathbf{y}_j$  of data in design  $\mathbf{D}_j$ , and the conditional probability of an excursion is

$$p_{\mathbf{u}}(\mathbf{y}_j, \mathbf{D}_j, \mathcal{Y}_{j-1}) = P(\xi_{\mathbf{u}} \leq t | \mathbf{y}_j, \mathbf{D}_j, \mathcal{Y}_{j-1}). \quad (8)$$

The notation in (7) indicates that the EIBV is an expectation with respect to the random data  $\mathbf{y}_j$  for design  $\mathbf{D}_j$ , conditional on the history of sampling results  $\mathcal{Y}_{j-1}$ .

The criterion for selecting design  $\mathbf{D}_j$  and then getting data  $\mathbf{y}_j$  at stage  $j = 1, \dots, J$ , is based on the minimum EIBV computed for all designs in a candidate waypoint set denoted  $\mathcal{D}_j$ . We have

$$\mathbf{D}_j = \text{argmin}_{\mathbf{D}'_j \in \mathcal{D}_j} \text{EIBV}(\mathbf{D}'_j). \quad (9)$$

Using expressions similar to that of [28], the EIBV in (7) can be evaluated in closed form. Denoting the variance reduction from data by  $\mathbf{V}_j = \mathbf{G}_j \mathbf{F}_j \mathbf{S}_{j-1}$ , see (3), the EIBV becomes

$$\begin{aligned} \text{EIBV}(\mathbf{D}'_j) &= \sum_{i=1}^n \text{EBV}_{\mathbf{u}_i}(\mathbf{D}'_j) \\ \text{EBV}_{\mathbf{u}_i}(\mathbf{D}'_j) &= \Phi_2 \left( \begin{bmatrix} t \\ -t \end{bmatrix}; \begin{bmatrix} m_{j-1}(i) \\ -m_{j-1}(i) \end{bmatrix}, \mathbf{W}_j(i, i) \right) \end{aligned} \quad (10)$$

where  $\Phi_2$  denotes the bivariate Gaussian cumulative distribution function, and with

$$\begin{aligned} \mathbf{W}_j(i, i) &= \begin{bmatrix} T(i, i) & -V_j(i, i) \\ -V_j(i, i) & T(i, i) \end{bmatrix} \\ T(i, i) &= S_j(i, i) + V_j(i, i). \end{aligned}$$

We next give some intuition for this EIBV criterion. Fig. 4 illustrates a Gaussian PDF (left) representing the current knowledge about salinity at some location. In this case it is standardized so that

$$Z_1 = \frac{\xi_{\mathbf{u}_i} - m_{j-1}(i)}{\sqrt{S_{j-1}(i, i)}}$$

for location  $\mathbf{u}_i$ . The scaled threshold  $t - m_{j-1}(i)$  is shown as a vertical line. With variance  $s_{j-1}^2(i) = S_{j-1}(i, i)$ , the current BV =  $p(1 - p)$ ,  $p = \Phi(\xi_{\mathbf{u}_i}; m_{j-1}(i), s_{j-1}^2(i))$  is also displayed.

We can collect data and get more information. The expected BV (EBV) at this location is then available as a cumulative probability as indicated in Fig. 4 (right). The EBV depends on the mean value relative to the threshold. Assume that the mean is lower, meaning that the threshold  $t - m_{j-1}(i)$  moves to the right in the left display. Then the BV decreases, and the EBV illustrated in the right display also decreases as the vertical line moves right and the horizontal line moves down. The EBV is further smallest when there is much negative correlation in the

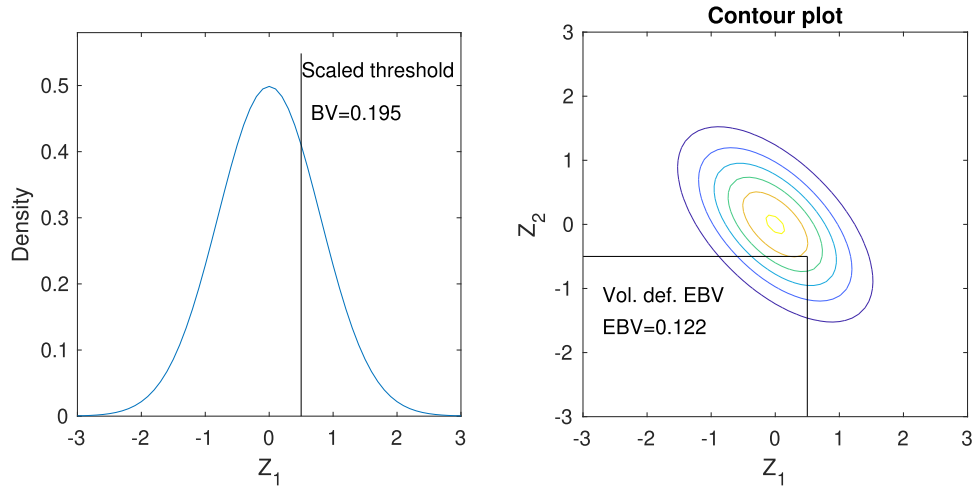


Fig. 4. Left: Density curve represents the current knowledge at a selected location, while the vertical line indicates the threshold. The Bernoulli variance (BV) is indicated. Right: EBV calculation involves bivariate Gaussian cumulative probabilities, which is the volume below the contours in the bottom left region.

---

**Algorithm 1: Informative Myopic Sampling Algorithm.**


---

**Initialization:**  $m_0, S_0, t, \mathcal{Y}_0 = \emptyset, \mathcal{D}_1$   
 $j = 1$   
**while**  $j \leq N_{steps}$  **do**  
  **Plan:** Evaluate  $EIBV(D'_j)$  for all  $D'_j \in \mathcal{D}_j \triangleright (7)$  and (10)  
   $D_j = \operatorname{argmin}_{D'_j \in \mathcal{D}_j} EIBV(D'_j) \triangleright (9)$   
  Go to design  $D_j$  with the AUV, set design matrix  $F_j$ , form set  $\mathcal{D}_{j+1}$ .  
  **Sense:** Gather in situ AUV data  $y_j$  according to design  $D_j$ .  
   $\mathcal{Y}_j = (\mathcal{Y}_{j-1}, y_j)$ .  
  **Update :**  $G_j = S_{j-1} F_j^T (F_j S_{j-1} F_j^T + R_j)^{-1}$   
   $m_j = m_{j-1} + G_j (y_j - F_j m_{j-1})$ ,  
   $S_j = S_{j-1} - G_j F_j S_{j-1} \triangleright (3)$   
   $j = j + 1$   
**end while**

---

density in Fig. 4 (right). From matrix  $W_j(i, i)$  in (11), we see that this occurs when the variance reduction  $V_j(i, i)$  is large compared with  $S_j(i, i) + V_j(i, i)$ . The bivariate  $\Phi_2$  calculation in (10) is somewhat costly, and if the correlation term is small, one could approximate it with two univariate calculations to gain computational efficiency.

Previous research has demonstrated the possibility of using EIBV as the design criterion for AUV adaptive sampling in 2-D domains [16]. We next explain how we build on this to construct effective AUV operations in 3-D adaptive sampling plans.

#### IV. PATH PLANNING ALGORITHM

##### A. Adaptive Sampling

The GRF model updating in (3) and closed form EIBV calculation in (10) enable information-based adaptive AUV sampling. We summarize the approach in Algorithm 1.

Note that as outlined this defines a myopic or greedy approach to adaptive sampling. This is not necessarily optimal. The myopic evaluation is done by taking the expectation of data at this stage only, without anticipation of what future sampling efforts might bring. The optimal solution to the sequential sampling design problem would also account for the sampling efforts at future stages. However, from the mathematical and computational setting, it is not feasible to find the optimal design strategy because it involves combinatorial growth of possible paths requiring intermixed optimization and expected values. Instead, one often resorts to the outlined myopic strategy. More nuanced approaches exist for doing longer-horizon search, for instance variants of Markov decision processes (MDPs) or partially observed MDPs [29], rapidly exploring random trees [30] or those based on genetic algorithms [31]. Such approaches will typically perform better than the myopic heuristic in situations with forbidden regions or with high collision risks, but it is not easy to use these in large-scale computations onboard the AUV. Further, restricted Monte Carlo search or pruning of paths, these nonmyopic approaches will not necessarily improve performance compared with a myopic search on the regular waypoint graph case [16]. We will limit scope to the myopic calculations (Algorithm 1) in this work.

For the 3-D application we consider here, the sequential sampling is restricted to a path embedded on a predefined grid of waypoints. In practice, the EIBV is computed for a set of neighborhood waypoint locations, meaning that the candidate design  $D'_j$  must be among those possible designs defining  $\mathcal{D}_j$ .

For small AUVs and large field, it might be possible to move the AUV wherever it needs to be. However, this might lead to an excess of manoeuvring time for the operation. To foster efficiency of the autonomous sampling process, a smooth-filtering method is applied to achieve AUV-friendly path planning (Algorithm 2). It first selects neighboring locations, and two vectors will be formed. Vector  $b_1$  is defined from the previous location to the current location, whereas vector  $b_2$  is from the current location to the potential candidate locations. Next, the inner products between these two vectors is calculated, and

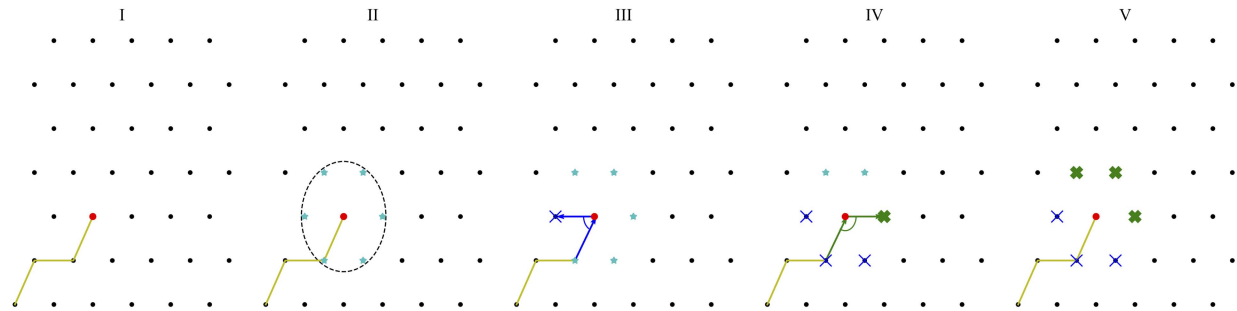


Fig. 5. Smooth path planning. I: Arrive at the current location. II: Search all neighboring locations. III, IV: Compute inner products. V: Select qualified candidate locations. Blue thin crosses indicate the abandoned locations, whereas the green thick crosses indicate the filtered locations.

---

**Algorithm 2: Smooth-Filtering Algorithm.**


---

**Require:**  $D_{j-1}, D_{j-2}$   
 $D^* = \{u \in \mathcal{M} \text{ such that } |u - D_{j-1}| < \text{neighboring distance}\}$   
 $\vec{b}_1 = D_{j-1} - D_{j-2}$   
 $i = 1$   
**while**  $i \leq N_{D^*}$  **do**  
 $\vec{b}_2 = D_i^* - D_{j-1}$   
**if**  $\vec{b}_1 \cdot \vec{b}_2 < 0$  **then**  
 Abandon  $D_i^*$ .  
**end if**  
 $i = i + 1$   
**end while**  
 $D_j = D^*$

---

only candidate locations with positive inner products will be considered for EIBV evaluation.

A map view version of the smooth-filtering is depicted on a 2-D waypoint graph in Fig. 5. In 3-D, the principle is the same, except that it is expanded to include the vertical candidate locations as well. This path smooth-filtering algorithm is effective since it removes locations which might require a hydrobatic maneuver to go there [32]. The smooth-filtered trajectory further avoids time-consuming turning which would increase the traveling time and introduce location inaccuracy.

## V. SIMULATION STUDY

To compare the performance between some existing algorithms and the 3-D myopic algorithm that we have developed here, a simulation study is conducted. We next describe the case, present the various methods, and discuss results.

### A. Simulation Setup

We use data from the numerical ocean model SINMOD as a reference for specifying realistic trends and variabilities for the oceanographic fjord-river water masses. Fig. 6 shows the average surface salinity field predicted for the first week in May using SINMOD. Four outlets from the river are recognized. The salinity variation from the river mouth to the ocean changes dramatically from bins of  $[0, 3]$  to  $[28, 30]$  ppt. The boundary between the freshwater and the more saline fjord water is clearly depicted by the contours.

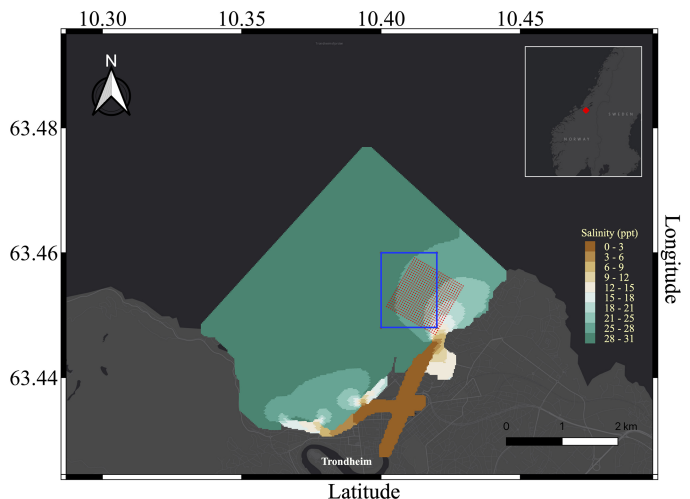


Fig. 6. Regional average surface salinity prediction in May 2021 from SINMOD. The blue rectangle indicates the designated simulation area (Section V), and the red dotted regions indicate the waypoint graph used in the field deployment (Section VI). The grid consists of  $25 \times 25$  nodes in each lateral axis and 5 layers in depth. *Courtesy of SINTEF Ocean and ESRI basemap.*

To narrow down the focus on mapping the front of the river plume in 3-D, a smaller region of interest in the easternmost part is selected (see blue rectangle in Fig. 6). Five depth layers 0.5, 1.0, 1.5, 2.0, 2.5 m are used.

A 3-D GRF benchmark field is created based on the data extracted from SINMOD on the desired simulation region. The mean values are set from averaging SINMOD data. The coefficients used in the Matérn covariance kernel are specified as  $\sigma = 0.71$ ,  $\phi_1 = 0.008$ ,  $\phi_2 = 2.25$ , and  $r = 0.2$ .

Fig. 7 shows one realization from our GRF model with the specified mean and covariance model. This is regarded as the ground truth in the simulation. There is clearly river plume areas to the south-east and near the surface, and realistic variability in salinity extent with some mixing of water masses, indicating that the GRF model emulates the physical phenomenon rather well.

### B. Simulation Approaches

We next describe two additional sampling strategies that are compared with our suggested 3-D adaptive sampling method. In

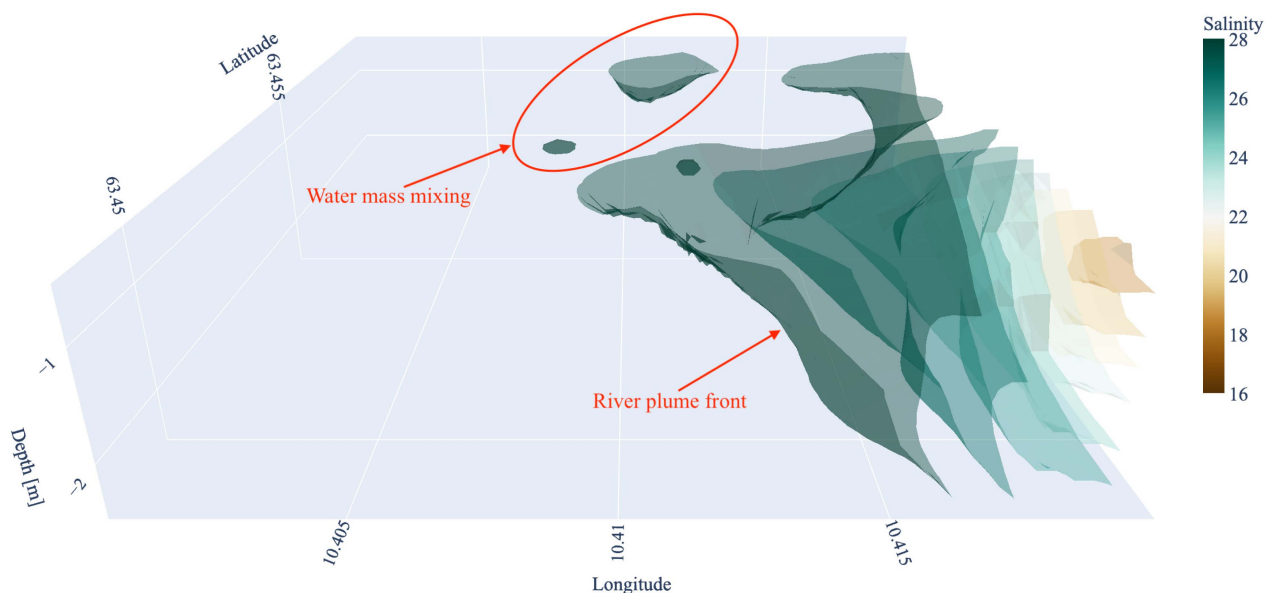


Fig. 7. One benchmark salinity field used in the simulation study. Some water blobs are shown on the north side of the region.

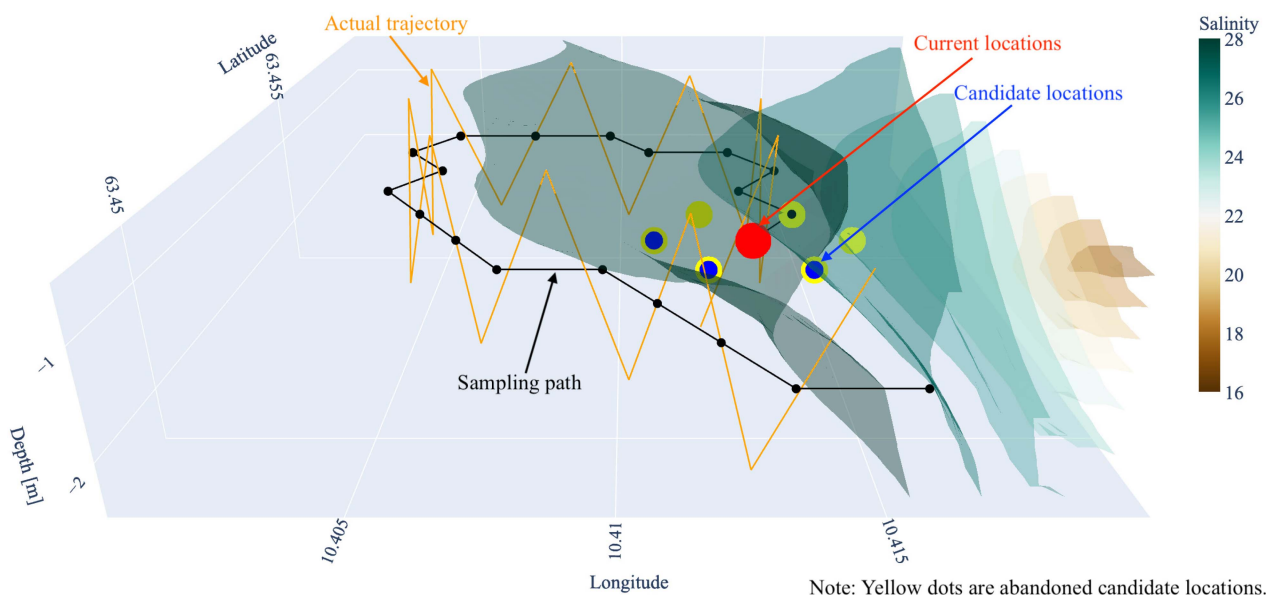


Fig. 8. Adaptive myopic 2-D algorithm illustration. The outmost envelope shows the estimated boundary after sampling 20 locations. Note that the yoyo pattern is shown as an illustration. It can be denser in the actual setting.

all three, the GRF proxy model provides an easy way to update the knowledge of the field by measuring the data at specified locations. The differences occur in how the data is included in the on-board computing and in what sampling strategy is used to explore the domain. When we compare results of the various approaches, they will be influenced by the sampling methodology used.

1) *Adaptive Myopic 2-D*: For the adaptive myopic 2-D, the AUV is only moving adaptively in the middle layer with the myopic strategy. It updates the entire field based on the data obtained from the middle layer at 1.5 m depth. In practice, the AUV needs to calibrate its navigational errors

by constantly popping up onto the surface and request accurate GPS locations and dive back to the place where it should continue. This is achieved by a yoyo pattern, as shown in Fig. 8.

2) *Nonadaptive Lawnmower*: For the nonadaptive lawnmower, Fig. 9 shows that the AUV will follow a predefined 3-D lawnmower pattern. In the lateral direction, the surface-projected trajectory will be a typical lawnmower manoeuvre. To extend it into 3-D, a vertical yoyo maneuver is added in addition to the lateral lawnmower. This preprogrammed method requires no statistical computations at waypoints, and it uncovers the field with large coverage. But the approach is usually time-consuming

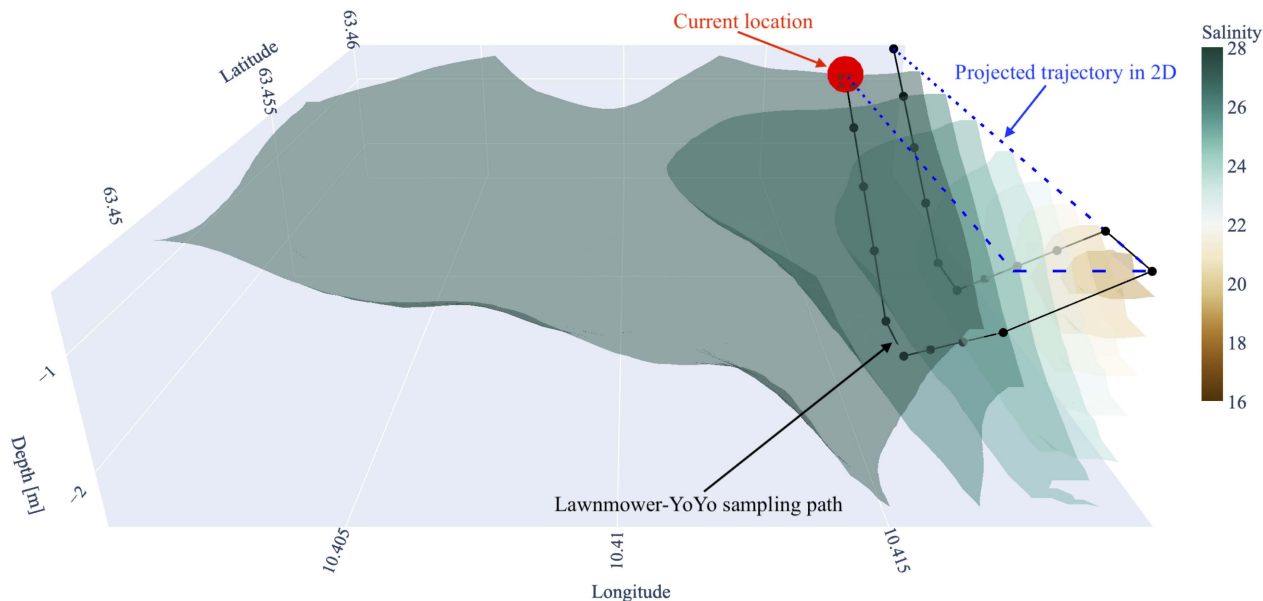


Fig. 9. Lawnmower-yoyo maneuver illustration. The estimated boundary after observing 20 sampling locations is shown as the outermost envelope.

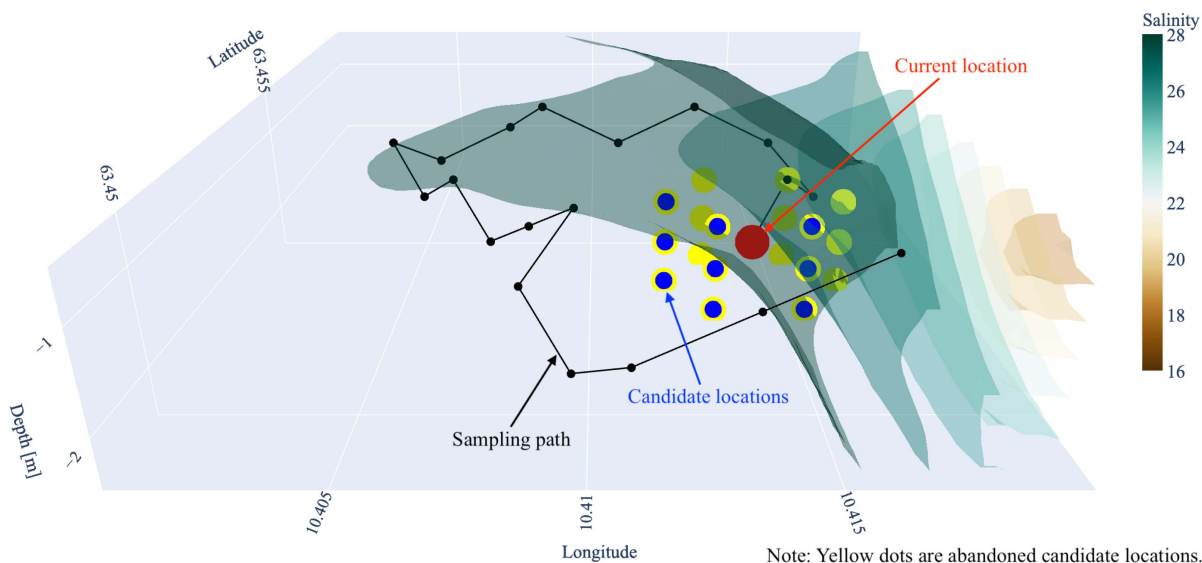


Fig. 10. Adaptive myopic 3-D sampling illustration. The outermost envelope shows the estimated river plume front after sampling 20 locations with the adaptive myopic 3-D path planning.

and inefficient in finding interesting features as it does not adapt to the data.

3) *Adaptive Myopic 3-D*: Our suggested adaptive myopic 3-D strategy extends the potential candidate sampling locations from one layer to include multiple layers. Therefore, it adapts to the field data with a much wider perspective. It is further both energy-efficient and time-efficient. One example of the adaptive 3-D myopic path planning is depicted in Fig. 10. One can see that at each stage, candidate locations will be generated in three dimensions. Only a few (shown as blue in Fig. 10) will be selected for the EIBV calculation due to the constraints of AUV maneuverability.

C. Simulation Results and Discussion

Figs. 8–10 show how each strategy behaves for one specific generated salinity field. To remove random effects, results of 100 replicate simulation results are averaged and shown in Fig. 11. At each time step of the runs, integrated Bernoulli variance (IBV), root-mean-squared error (RMSE), variance reduction and distance traveled are monitored for comparison of the three strategies.

The IBV indicator shows that the Lawnmower-yoyo pattern has the slowest reduction of the three strategies. However, it goes down quickly when the robot is in the area of interest, i.e., the boundary region or the front of the river plume, performing

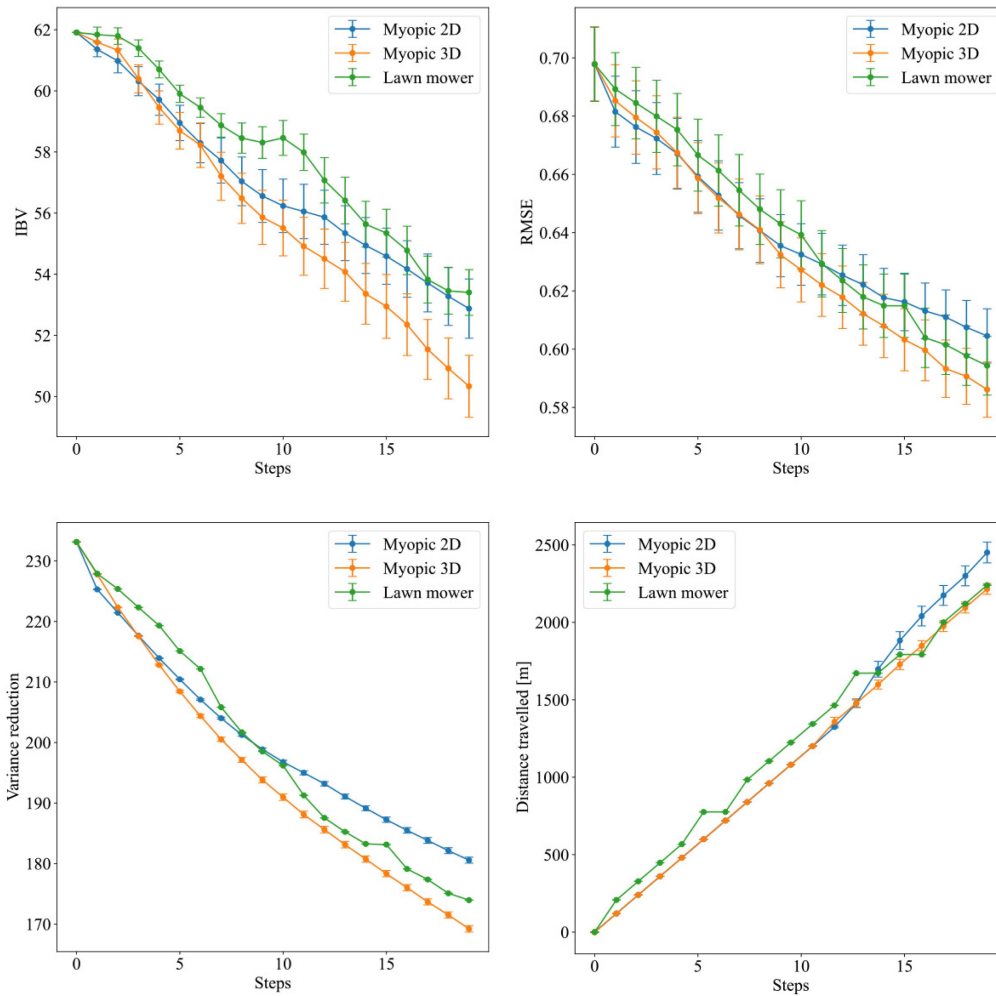


Fig. 11. Average results from 100 replicate simulations for 20 sampling locations. The standard error is depicted as vertical lines.

better than myopic 2-D after about 15 iterations (The same holds for RMSE and variance reduction.) This occurs because the lawn mower strategy can get lucky and the AUV runs into interesting parts of the domain, but it can also miss this entirely in the given time window. Even though the myopic 3-D strategy is guided by EIBV reduction, it also achieves large reduction in RMSE and variance, and more so than the other methods. It performs better than the 3-D lawnmower strategy because it explores new parts of the domains and in doing so avoids locations that are highly correlated to the ones already sampled.

With the same starting location and about the same traveled distance (see Fig. 11, lower right), the 3-D version of the myopic planning reveals the most information of the field within the three strategies. The flexibility in 3-D enables the AUV to both explore and exploit the environment effectively.

## VI. AUV EXPERIMENTS IN THE NIDELVA PLUME

We next describe and show results of AUV experiments done in late Spring 2021 to map the Nidelva River plume, Trondheim, Norway. The adaptive AUV experiments were conducted on 6 July 2021. Before that, we gathered various complementary data. The phone footage on 27 May shows a visible river plume (see

Fig. 12). A satellite image on 2 June (see Fig. 13) shows how the river plume area is unfolded by pollen flushed away by the river in the spring season. That matches very well with the phone footage (see Fig. 12). Such data motivate AUV sampling for calibration, improved resolution, and 3-D characterization.

### A. Experiment Setup

1) *Discretize the Grid*: Computational constraints and practical matters lead to a  $25 \times 25 \times 5$  grid discretization within the  $1 \text{ km} \times 1 \text{ km} \times 2 \text{ m}$  box region overlapping the river plume area as shown in Fig. 6 (red dots). We concentrate our effort on the near-surface regions (depth smaller than 2.5 m) because ocean model data and observations made during an initial AUV transect (see Fig. 14) show that the freshwater river plume tends to float close to the surface regions [1].

2) *Building the Prior*: To form a prior, we use SINMOD data as a core building block. First, we allocate mean values to each 3-D grid node, extracted from averages over many SINMOD runs. Second, we calibrate these mean values in a regression model using AUV data from a preliminary transect survey. A linear regression model  $y_{\mathbf{u}_k} = \beta_0 + \beta_1 y_{\mathbf{u}_k}^{\text{SINMOD}}$  is fitted, where  $\mathbf{u}_k$  indicate locations

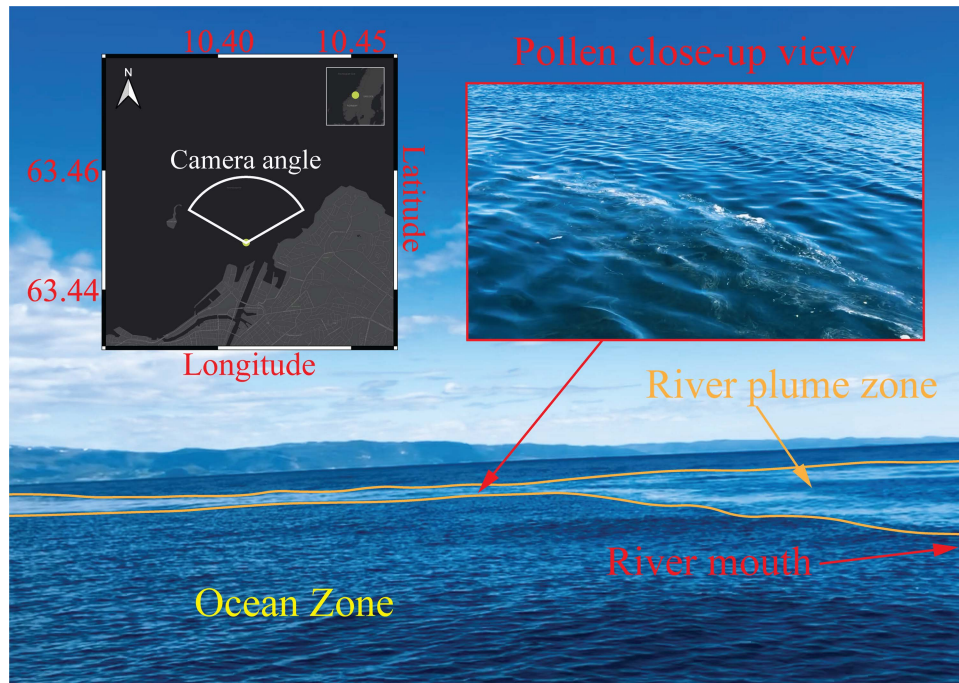
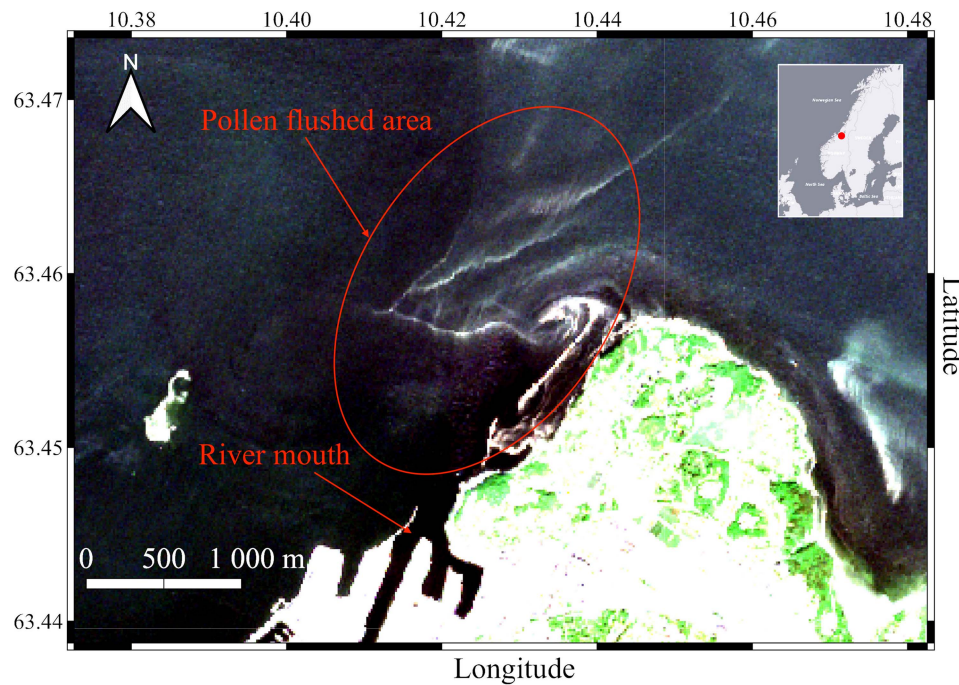


Fig. 12. River plume zone captured by mobile phone on 27 May 2021. The camera perspective is shown as the white fan on the left corner which indicates the area where the plume occurs.



Satellite image captured by Sentinel-2 on June-2nd 2021, courtesy of Copernicus Sentinel data [2021]

Fig. 13. Satellite image captured on 2 June 2021, showing the visible river plume thanks to the pollen flushed away by the river.

of transect line AUV data  $y_{u_k}$  and SINMOD data  $y_{u_k}^{SINMOD}$ . The fitted coefficients  $\hat{\beta}_0$ ,  $\hat{\beta}_1$  adjust the entire field, and  $\hat{\beta}_0 + \hat{\beta}_1 y_{u_k}^{SINMOD}$  provides the prior mean in the onboard model used in the AUV deployment.

The coefficients for the Matérn kernel are approximated using empirical variograms of the AUV data collected from the initial survey. They are specified to  $\sigma = 2$ ,  $\phi_1 = 0.011$ ,  $\phi_2 = 0.94$ , and  $r = 0.55$ . Careful assessment of these parameters is important

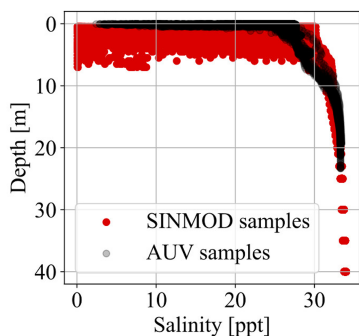


Fig. 14. Salinity versus depth plot from AUV in situ measurements and from SINMOD prediction. Both SINMOD and the in situ measurements show that most salinity variation happens close to the surface.



Fig. 15. LAUV Roald is taking a shower after the heavy duty.

when it comes to sharpening the performance of the adaptive sampling algorithm such that it recognizes the boundary more agilely. However, further tweaking of these parameters are out of the scope of this work.

3) *AUV Deployment*: LAUV Roald (see Fig. 15) from the Applied Underwater Robotics Laboratory at NTNU was employed in the Nidelva missions. All the essential scripts were integrated onboard on the backseat NVIDIA Jetson TX2 CPU. For hardware and software in the loop testing and the actual deployment we relied on the framework developed by [12]. The implementation of Algorithm 1 and 2 requires robot operating systems (ROS) [33] and a software bridge to the LAUV, running

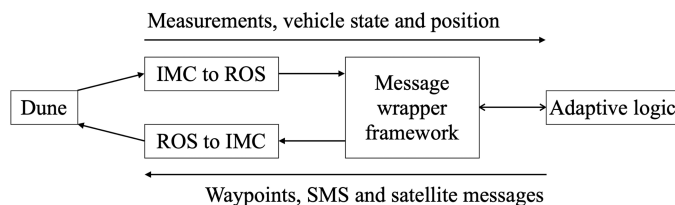


Fig. 16. Main software components in the communication between the adaptive code and the vehicle. DUNE [34] is running on the main CPU of the AUV while the IMC [35] messages are transmitted via TCP [37] to an auxiliary CPU, where ROS [33] and the adaptive code is run.

DUNE (DUNE :Unified Navigation Environment [34]) embedded and communicating over the intermodule communication (IMC) message protocol [35].

The software bridge between ROS and IMC was adapted from the Swedish Maritime Robotics Centers implementation of an ROS-IMC bridge [36]<sup>1</sup> to include messages going from ROS to the vehicle. In addition, a wrapper for the vehicle IMC messages was used, enabling easy interaction between the adaptive software and the vehicle. The communication bridge and framework between ROS and IMC use the same back-seat interface as [15], with IMC messages being transmitted over Transmission Control Protocol (TCP) [37] between the main CPU and the auxiliary CPU in the AUV. The adaptive code is run in the auxiliary CPU to preserve the integrity of the main CPU. For illustration, a flowchart containing the main software components is presented in Fig. 16.

### B. Experiment Results and Discussion

Fig. 17 shows the posterior EPs after assimilating all the AUV measurements from the adaptive mission. When the EP is close to 1, it is classified as river water, while ocean water has probabilities close to 0. Some parts of the domain are still unexplored and have intermediate probabilities. In its adaptive sampling efforts to distinguish the water masses, the AUV travels between different layers and traverse the lateral domain. The sampling mainly takes place in the top three layers that mirror the buoyant river plume assumption, but it dips down to 2 and 2.5 m. The adaptive behavior guides the agent to be within the boundary region instead of putting too much effort on either side of the front. According to the updated field, there appears to be patches of river waters going down to 1 and 1.5 m, but most river water is near the surface.

In Fig. 18, we compare prior and posterior EPs for the top two layers. Clearly, the AUV reveals a bigger plume region than what is predicted by the SINMOD prior model. At 1.0 m there appears to be water mass separation. This kind of separation is likely very heterogeneous in space and time, and the displayed results only show predicted conditions at the day of the mission.

<sup>1</sup>[Online]. Available: [https://github.com/smarc-project/imc\\_ros\\_bridge](https://github.com/smarc-project/imc_ros_bridge)

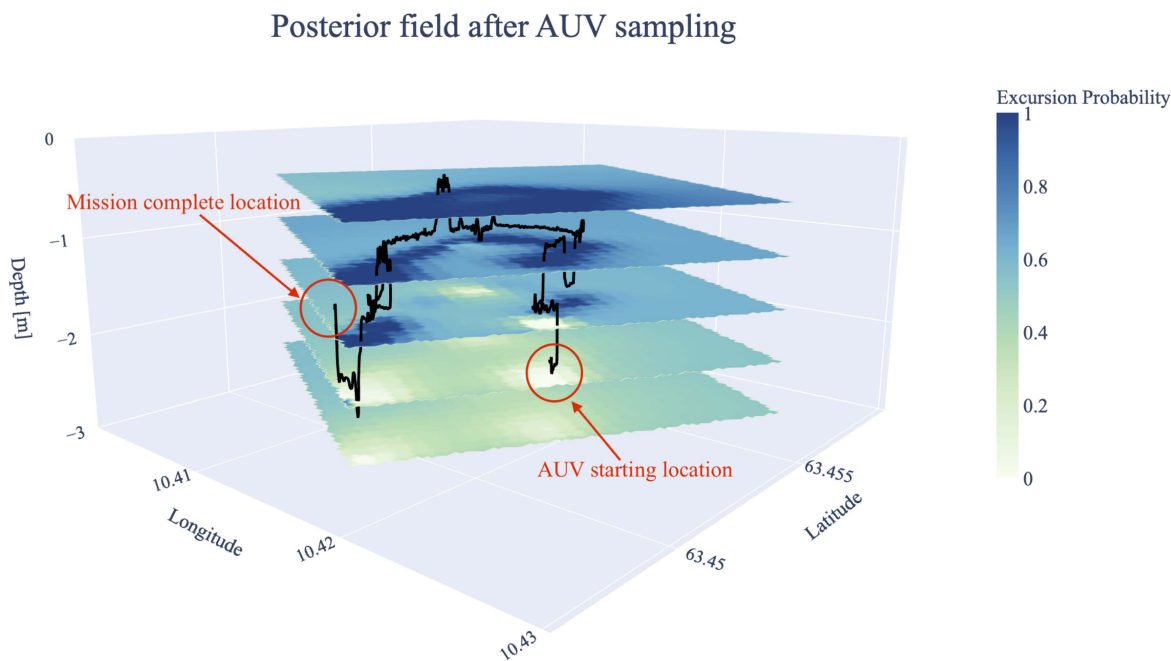


Fig. 17. Excursion probability for the posterior field. It describes how similar the water mass is to the river water. Values near 1 (blue) represents river water, while 0 (white) represents ocean water.

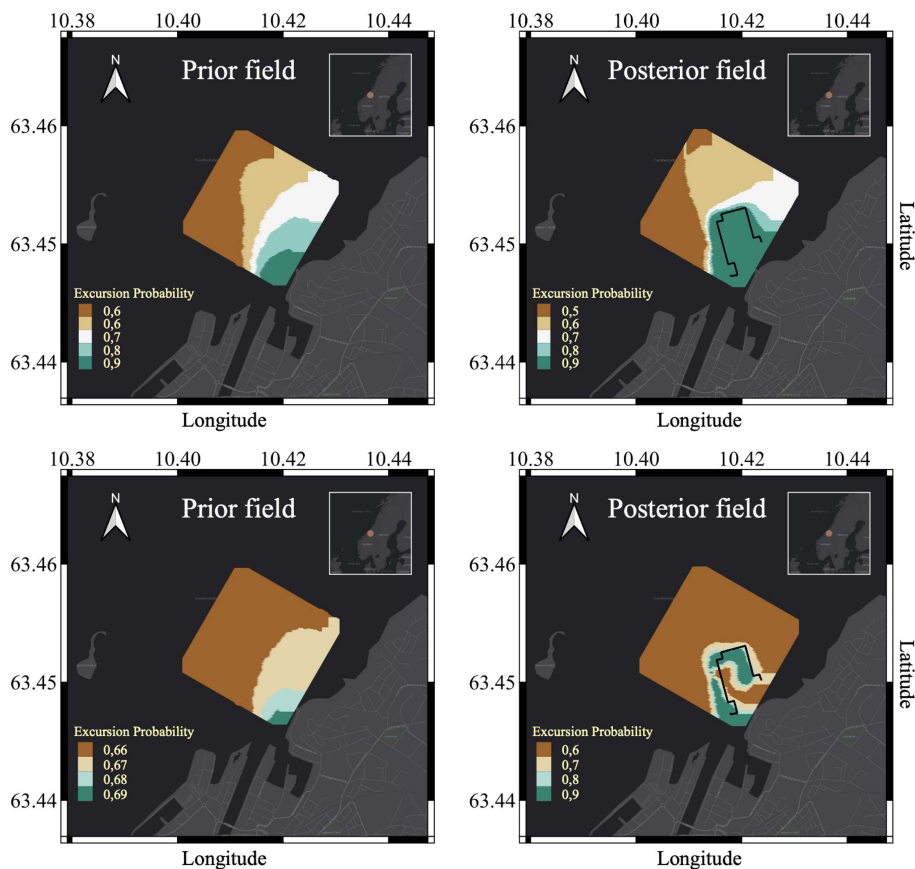


Fig. 18. Excursion probability comparison for the prior field (left) and the posterior field (right) at 0.5 m depth (top) and 1.0 m depth (bottom). The AUV trajectory is shown as the black line in the right column.

## VII. CONCLUSION

The main contribution of this work is to apply Gaussian random field models for 3-D north-east-depth domains in the context of adaptive sampling with real-time computation and maneuverability routines on a robotic vehicle. The adaptive sampling routine presented here is tailored to frontal systems, and it relies on reduction of the EIBV. We conducted a simulation study comparing the suggested approach with more standard approaches. Results demonstrate the capability of the adaptive myopic 3-D sampling in a field deployment. The AUV managed to distinguish the different water masses in a river plume in a Norwegian fjord-river system.

River plumes are influenced by many factors such as winds, waves, and tides, and we could likely model statistical correlations more sensibly by using a nonstationary Gaussian random field prior [38]. Our method uses ocean model data to build a reasonable prior model of the salinity field in 3-D. However, when this type of information is lacking, the prior belief can also be constructed based on other data, possibly satellite imagery or buoy information. As AUV data are rather sparse, there is likely much to gain by using spatially covering physical modeling data and satellite data, as this allows a better initial model for sampling.

The time variation will play an important role if the AUV deployment lasts longer. This is naturally the case when the frontal region gets bigger and the distance traveled by the AUV increases. In long-term deployments it will also be important to capture such temporal effects [39]. The current myopic philosophy works well for a small river plume. As the plume gets bigger, or one has interest in capturing subregional plumes, there is likely some gain by using strategies that anticipate many stages [30], [31] or in using ocean physics for the 3-D navigation [40]. Other opportunities stem from using adaptive sampling in a cooperative fleet as discussed in [41].

## ACKNOWLEDGMENT

The authors would like to thank AURLab NTNU for the support, collaboration, and easy access to testing equipment. The authors would also like to thank K. A. Skarpnes for his help during all the field-trials in 2021 and SINTEF Ocean for supplying SINMOD data.

## REFERENCES

- [1] A. R. Horner-Devine, R. D. Hetland, and D. G. MacDonald, "Mixing and transport in coastal river plumes," *Annu. Rev. Fluid Mechanics*, vol. 47, no. 1, pp. 569–594, 2015.
- [2] S. Constantin, D. Doxaran, and S. Constantinescu, "Estimation of water turbidity and analysis of its spatio-temporal variability in the Danube River plume (Black Sea) using modis satellite data," *Continental Shelf Res.*, vol. 112, pp. 14–30, 2016.
- [3] A. A. Osadchiv and P. O. Zavialov, "Lagrangian model of a surface-advected river plume," *Continental Shelf Res.*, vol. 58, pp. 96–106, 2013.
- [4] S. Zheng, W. Guan, S. Cai, X. Wei, and D. Huang, "A model study of the effects of river discharges and interannual variation of winds on the plume front in winter in Pearl River Estuary," *Continental Shelf Res.*, vol. 73, pp. 31–40, 2014.
- [5] F. M. Falcieri, A. Benetazzo, M. Sclavo, A. Russo, and S. Carniel, "Po river plume pattern variability investigated from model data," *Continental Shelf Res.*, vol. 87, pp. 84–95, 2014.
- [6] R. Mendes et al., "Observation of a turbid plume using modis imagery: The case of Douro estuary (Portugal)," *Remote Sens. Environ.*, vol. 154, pp. 127–138, 2014.
- [7] G. S. Saldías, J. L. Largier, R. Mendes, I. Pérez-Santos, C. A. Vargas, and M. Sobarzo, "Satellite-measured interannual variability of turbid river plumes off Central-Southern Chile: Spatial patterns and the influence of climate variability," *Prog. Oceanogr.*, vol. 146, pp. 212–222, 2016.
- [8] E. Park and E. M. Latrubesse, "Modeling suspended sediment distribution patterns of the Amazon River using Modis data," *Remote Sens. Environ.*, vol. 147, pp. 232–242, 2014.
- [9] J. Hwang, N. Bose, and S. Fan, "AUV adaptive sampling methods: A review," *Appl. Sci.*, vol. 9, no. 15, 2019, Art. no. 3145.
- [10] E. Fiorelli, N. E. Leonard, P. Bhatta, D. A. Paley, R. Bachmayer, and D. M. Fratantoni, "Multi-AUV control and adaptive sampling in Monterey Bay," *IEEE J. Ocean. Eng.*, vol. 31, no. 4, pp. 935–948, Oct. 2006.
- [11] T. O. Fossum et al., "Toward adaptive robotic sampling of phytoplankton in the coastal ocean," *Sci. Robot.*, vol. 4, no. 27, 2019, Art. no. aav3041.
- [12] T. Mo-Bjørkelund, T. O. Fossum, P. Norgren, and M. Ludvigsen, "Hexagonal grid graph as a basis for adaptive sampling of ocean gradients using AUVs," in *Proc. IEEE Glob. Oceans 2020: Singapore–U.S. Gulf Coast*, 2020, pp. 1–5.
- [13] P. Rogowski, E. Terrill, and J. Chen, "Observations of the frontal region of a buoyant river plume using an autonomous underwater vehicle," *J. Geophysical Res.: Oceans*, vol. 119, no. 11, pp. 7549–7567, 2014.
- [14] Y. Zhang, J. G. Bellingham, J. P. Ryan, B. Kieft, and M. J. Stanway, "Autonomous four-dimensional mapping and tracking of a coastal upwelling front by an autonomous underwater vehicle," *J. Field Robot.*, vol. 33, no. 1, pp. 67–81, 2016.
- [15] J. Pinto, R. Mendes, J. C. B. da Silva, J. M. Dias, and J. B. de Sousa, "Multiple autonomous vehicles applied to plume detection and tracking," in *Proc. IEEE OCEANS Conf. - MTS/IEEE Kobe Techno-Oceans*, 2018, pp. 1–6.
- [16] T. O. Fossum, C. Travelletti, J. Eidsvik, D. Ginsbourger, and K. Rajan, "Learning excursion sets of vector-valued Gaussian random fields for autonomous ocean sampling," *Ann. Appl. Statist.*, vol. 15, no. 2, pp. 597–618, 2021.
- [17] R. Cui, Y. Li, and W. Yan, "Mutual information-based multi-AUV path planning for scalar field sampling using multidimensional RRT\*," *IEEE Trans. Syst., Man, Cybern. Syst.*, vol. 46, no. 7, pp. 993–1004, Jul. 2016.
- [18] P. Stankiewicz, Y. T. Tan, and M. Kobilarov, "Adaptive sampling with an autonomous underwater vehicle in static marine environments," *J. Field Robot.*, vol. 38, no. 4, pp. 572–597, 2021.
- [19] A. Sousa et al., "LAUV: The man-portable autonomous underwater vehicle," *IFAC Proc. Volumes*, vol. 45, no. 5, pp. 2–274, 2012.
- [20] D. Slagstad and T. A. McClimans, "Modeling the ecosystem dynamics of the Barents Sea including the marginal ice zone: I physical and chemical oceanography," *J. Mar. Syst.*, vol. 58, no. 12, pp. 1–18, 2005.
- [21] P. F. Lermusiaux, "Uncertainty estimation and prediction for interdisciplinary ocean dynamics," *J. Comput. Phys.*, vol. 217, no. 1, pp. 176–199, 2006.
- [22] M. Lin and C. Yang, "Ocean observation technologies: A review," *Chin. J. Mech. Eng.*, vol. 33, no. 1, pp. 1–18, 2020.
- [23] S. Martin, *An Introduction to Ocean Remote Sensing*. Cambridge, U.K.: Cambridge Univ. Press, 2014.
- [24] F. A. Al-Wassai and N. V. Kalyankar, "Major limitations of satellite images," 2013, *arXiv:1307.2434*.
- [25] S. Kemna, O. Kroemer, and G. S. Sukhatme, "Pilot surveys for adaptive informative sampling," in *Proc. IEEE Int. Conf. Robot. Autom.*, 2018, pp. 6417–6424.
- [26] F. S. Longman, L. Mihaylova, and L. Yang, "A Gaussian process regression approach for fusion of remote sensing images for oil spill segmentation," in *Proc. 21st Int. Conf. Inf. Fusion*, 2018, pp. 62–69.
- [27] N. Cressie and C. K. Wikle, *Statistics for Spatio-Temporal Data*. Hoboken, NJ, USA: Wiley, 2015.
- [28] C. Chevalier, J. Bect, D. Ginsbourger, E. Vazquez, V. Picheny, and Y. Richet, "Fast parallel Kriging-based stepwise uncertainty reduction with application to the identification of an excursion set," *Technometrics*, vol. 56, no. 4, pp. 455–465, 2014.
- [29] D. Silver and J. Veness, "Monte-Carlo planning in large POMDPs," in *Proc. 23rd Int. Conf. Neural Inf. Process. Syst.*, 2010, pp. 2164–2174.
- [30] C. Xiong, H. Zhou, D. Lu, Z. Zeng, L. Lian, and C. Yu, "Rapidly-exploring adaptive sampling tree\*: A sample-based path-planning algorithm for unmanned marine vehicles information gathering in variable ocean environments," *Sensors*, vol. 20, no. 9, 2020, Art. no. 2515.

- [31] M. Bresciani et al., "Path planning for underwater information gathering based on genetic algorithms and data stochastic models," *J. Mar. Sci. Eng.*, vol. 9, no. 11, 2021, Art. no. 1183.
- [32] S. Bhat, "Hydrobotics: Efficient and agile underwater robots," Ph.D. dissertation, Dept. Vehicle Maritime Eng., KTH Royal Inst. Technol., Stockholm, Sweden, 2020.
- [33] M. Quigley, "ROS: An open-source robot operating system," in *Proc. ICRA Workshop Open Source Softw.*, 2009, vol. 3, no. 3.2, p. 5.
- [34] J. Pinto, P. S. Dias, R. Martins, J. Fortuna, E. Marques, and J. Sousa, "The LSTS toolchain for networked vehicle systems," in *Proc. IEEE/MTS OCEANS Conf.*, Bergen, Norway, 2013, pp. 1–9.
- [35] R. Martins et al., "IMC: A communication protocol for networked vehicles and sensors," in *Proc. IEEE Oceans 2009 - Europe*, 2009.
- [36] S. Bhat et al., "A cyber-physical system for hydrobotic AUVs: System integration and field demonstration," in *Proc. IEEE/OES Auton. Underwater Veh. Symp.*, 2020, pp. 1–8.
- [37] V. Cerf and R. Kahn, "A protocol for packet network intercommunication," *IEEE Trans. Commun.*, vol. 22, no. 5, pp. 637–648, May 1974.
- [38] G.-A. Fuglstad, F. Lindgren, D. Simpson, and H. Rue, "Exploring a new class of non-stationary spatial Gaussian random fields with varying local anisotropy," *Statistica Sinica*, vol. 25, pp. 115–133, 2015.
- [39] K. H. Foss, G. E. Berget, and J. Eidsvik, "Using an autonomous underwater vehicle with onboard stochastic advection-diffusion models to map excursion sets of environmental variables," *Environmetrics*, vol. 33, 2022, Art. no. e27102.
- [40] C. S. Kulkarni and P. F. Lermusiaux, "Three-dimensional time-optimal path planning in the ocean," *Ocean Model.*, vol. 152, 2020, Art. no. 101644.
- [41] M. J. Kuhlman, D. Jones, D. A. Sofge, G. A. Hollinger, and S. K. Gupta, "Collaborating underwater vehicles conducting large-scale geospatial tasks," *IEEE J. Ocean. Eng.*, vol. 46, no. 3, pp. 785–807, Jul. 2021.



**Yaolin Ge** received the dual M.Sc. degrees in maritime engineering in 2020 from the KTH Royal Institute of Technology, Stockholm, Sweden, and Norwegian University of Science and Technology (NTNU), Trondheim, Norway, where he is currently working toward the Ph.D. degree in statistics with the Department of Mathematical Sciences.



**Jo Eidsvik** received the M.Sc. degree in applied mathematics from the University of Oslo, Oslo, Norway, in 1997, and the Ph.D. degree in statistics from the Norwegian University of Science and Technology (NTNU), Trondheim, Norway, in 2003.

He is currently a Professor of Statistics with NTNU. He has industry experience with the Norwegian Defence Research Establishment, Kjeller, Norway and with Equinor, Stavanger, Norway. His research interests include computational methods and sampling design approaches related to spatio-temporal statistics. He works mainly with applications from the earth sciences.



**Tore Mo-Bjørkelund** received the M.Sc. degree in marine cybernetics in 2017 from the Norwegian University of Science and Technology (NTNU), Trondheim, Norway, where he is currently working toward the Ph.D. degree in autonomous underwater systems.